Received: 28 March 2025 | Revised: 15 May 2025 | Accepted: 29 May 2025

DOI: 10.1002/inf2.70043

RESEARCH ARTICLE

WILEY

Bidirectional functionality of a modified PCBM layer: Enhancing perovskite photovoltaics beyond single-bandgap devices

Yonggui Sun[1] | **Qianyi Ma**[2] | **Fei Wang**[1] | **Xiaokang Sun**[1] | **Taomiao Wang**[1] | **Xianfang Zhou**[1] | **Qiannan Li**[1] | **Dawei Duan**[1] | **Tao Zhang**[1] | **Xiaoxi Huang**[1] | **Haoran Lin**[1] | **Jun Pan**[3] | **Wenzhu Liu**[4] | **Jingbai Li**[1] | **Annie Ng**[5] | **Chunming Yang**[2] | **Mingjian Yuan**[6] | **Tom Wu**[7] | **Hanlin Hu**[1]

[1]Hoffmann Institute of Advanced Materials, Postdoctoral Innovation Practice Base, Shenzhen Polytechnic University, Shenzhen, the People's Republic of China

[2]Shanghai Synchrotron Radiation Facility, Shanghai Advanced Research Institute, Chinese Academy of Sciences, Shanghai, the People's Republic of China

[3]Science and Education Integration College of Energy and Carbon Neutralization, Zhejiang University of Technology, Hangzhou, the People's Republic of China

[4]Research Center for New Energy Technology, Shanghai Institute of Microsystem and Information Technology, Chinese Academy of Sciences, Shanghai, the People's Republic of China

[5]Department of Electrical and Computer Engineering, School of Engineering and Digital Sciences, Nazarbayev University, Astana, Kazakhstan

[6]College of Chemistry, Nankai University, Tianjin, the People's Republic of China

[7]Department of Applied Physics, Hong Kong Polytechnic University, Hong Kong, the People's Republic of China

Correspondence

Jingbai Li, Hoffmann Institute of Advanced Materials, Postdoctoral Innovation Practice Base, Shenzhen Polytechnic University, Shenzhen, the People's Republic of China.
Email: lijingbai@szpu.edu.cn

Annie Ng, Department of Electrical and Computer Engineering, School of Engineering and Digital Sciences, Nazarbayev University, Astana 010000, Kazakhstan.
Email: annie.ng@nu.edu.kz

Chunming Yang, Shanghai Synchrotron Radiation Facility, Shanghai Advanced Research Institute, Chinese Academy of Sciences, Shanghai 201204 the People's Republic of China.
Email: yangcm@sari.ac.cn

Abstract

Metal electrode corrosion driven by halide migration and interfacial defects remains a significant bottleneck limiting the operational stability and photovoltaic performance of perovskite solar cells (PSCs), particularly in devices with varied bandgaps. Herein, we present a multifunctional interface engineering strategy by incorporating the IL 1-butylpyridinium tetrafluoroborate ($BPYBF_4$) into the PCBM electron transport layer to simultaneously address these issues. The BF_4^- anions coordinate with the Ag^+, forming a corrosion-resistant layer that mitigates iodine-induced degradation. Concurrently, the BPY^+ cations react with residual PbI_2 at the perovskite surface, inducing the formation of a 1D perovskite capping layer that effectively passivates interfacial defects and suppresses ion migration. Phase-transition process during film conversion was systematically investigated, revealing a gradual transformation of residual PbI_2 into a protective 1D perovskite structure upon $BPYBF_4$

Yonggui Sun, Qianyi Ma, and Fei Wang contributed equally to this work.

Hanlin Hu, Hoffmann Institute of Advanced Materials, Postdoctoral Innovation Practice Base, Shenzhen Polytechnic University, Shenzhen, the People's Republic of China.
Email: hanlinhu@szpu.edu.cn

Funding information
Nazarbayev University under Collaborative Research Program, Grant/Award Number: 211123CRP1613; Faculty Development Competitive Research Grants Program for 2024–2026, Grant/Award Number: 201223FD8801; Scientific Research Startup Fund for Spray-on Perovskite Photovoltaics R&D Center, Grant/Award Numbers: 602331011PQ, 2024ZDZX3079; Guangdong Basic and Applied Basic Research Foundation, Grant/Award Number: 2023A1515011677; Scientific and Technical Innovation Council of Shenzhen, Grant/Award Number: 20220812165832002; Research Projects of Department of Education of Guangdong Province, Grant/Award Number: 2023GCZX015; Innovation Team Project of Guangdong, Grant/Award Number: 2022KCXTD055; National Key R&D Program of China, Grant/Award Number: 2021YFA1601000; Shanghai Municipal Science and Technology Major Project; National Natural Science Foundation of China, Grant/Award Numbers: 12175295, U1932118

incorporation. Additionally, the presence of ionized PCBM enhances surface potential alignment, promoting efficient electron extraction and reducing non-radiative recombination losses. This strategy demonstrates broad applicability—not only enhancing the performance of 1.55 eV normal-bandgap PSCs but also achieving outstanding efficiency for wide-bandgap PSCs, with PCEs of 22.69% for 1.67 eV and 18.60% (certified at 17.75%) for 1.85 eV, respectively. This work provides a facile and scalable approach to simultaneously protect the electrode and stabilize the perovskite films, offering a promising strategy for varied bandgaps PSCs in both single-junction and tandem configurations.

KEYWORDS
1D/3D perovskite, Ag electrode, time-resolved GIWAXS, wide-bandgap

1 | INTRODUCTION

After over a decade of development, the power conversion efficiency (PCE) of single-junction perovskite solar cells (PSCs) has currently exceeded 26%.[1,2] Perovskite materials offer broad bandgap tunability, making them an ideal choice for both the front sub-cells and bottom sub-cells of tandem solar cells.[3–5] However, defects typically arise during the solution-based fabrication of perovskite films, manifesting on the film surface and at the grain boundaries. These defects serve as sites for non-radiative recombination of charge carriers, making the films susceptible to degradation from humidity, light, and heat—factors that severely compromise the stability of the devices.[6–8] Additionally, the enhancement of the PCE of PSCs remains limited by the high voltage loss which is primarily because significant carrier non-radiative recombination occurs at the electron extraction interface represented by perovskite-PCBM, along with the problem of interlayer energy level mismatch.[9,10] To address these challenges, numerous strategies have been developed, including additive engineering,[11] surface post-treatment engineering[12] and solvent engineering,[13] all aimed at eliminating defects on the surface and at the grain boundaries of perovskite films. These approaches are designed to enhance the overall performance of the devices, with a particular focus on improving stability. Among these strategies, the introduction of low-dimensional (LD) perovskites onto the surface of three-dimensional (3D) perovskites has proven effective in passivating surface and grain-boundary defects.[14–16] On one hand, the organic cations in LD perovskites act as a barrier to moisture intrusion, mitigating device degradation.[17,18] On the other hand, the stable LD structure inhibits the migration of halide and lead ions, further enhancing the device stability.[19] Due to their structural flexibility and significantly enhanced carrier-transport properties, one-dimensional (1D) perovskites stand out among LD structures, showing great promise in terms of research potential.[20] Ji et al. added Choline Acetate (CA) to the PbI_2 precursor solution and demonstrated that a 1D/3D heterojunction structure spontaneously

formed at the bottom of the perovskite layer via a two-step deposition method.[21] The 1D perovskite structure formed at the buried interface can not only serve as a protective layer but also introduce an electric dipole at the interface, thus facilitating the transport of hole carriers. The optimized 1D/3D device achieved a PCE of 24.03%, demonstrating a significant improvement. It also exhibited a minimal hysteresis effect and excellent stability. Chen et al. introduced 1,10-phenanthroline (Phen), a bidentate ligand with two lone pairs, onto the upper surface of 3D perovskite through a post-treatment method to form a 1D perovskite structure, aiming to passivate the surface defects of 3D perovskite.[22] The excellent surface passivation of 1D perovskite enables the modified perovskite film to exhibit stronger photoluminescence (PL) and longer decay time, simultaneously inhibiting ion migration. The device based on stacked 1D/3D structures achieved a PCE of 23.3%, which is superior to the 3D device, as well as demonstrating excellent operation stability. However, the post-treatment process increases the complexity of device fabrication and is not conducive to industrial applications. Moreover, many materials used to form 1D perovskite are either toxic or have complex synthesis steps. Therefore, it is of particular importance to select environmentally friendly and easily accessible materials as well as appropriate application methods.

Silver (Ag) is commonly used in inverted PSCs due to its suitable work function.[23] However, its inherent reactivity and corrosiveness toward perovskite materials can significantly compromise device stability.[24] The degradation of perovskite materials generates large amounts of iodine (I), which can react with low-work-function metal electrodes such as Ag, aluminum (Al), and copper (Cu). This reaction not only depletes the halogens in the perovskite structure but also corrodes the metal electrodes, forming compounds such as AgI, AlI_3, and CuI, which severely restrict the optoelectronic performance of the device.[25–27] To mitigate the mutual degradation between metal electrodes and perovskite materials, various materials have been employed as buffer layers to address cathode interface issues.[28,29] Among them, BCP is widely used due to its deep valence band, which effectively blocks hole carriers. However, its tendency to rapidly crystallize leads to accumulation on the PCBM surface, resulting in uneven coverage and insufficient protection against Ag corrosion induced by iodine.[30]

To address the formation of defects during the perovskite crystallization process and the detrimental Ag-I coordination that accelerates perovskite degradation, there is an urgent imperative to develop sustainable interfacial modification materials to mitigate these stability challenges. Ionic liquids (ILs), distinguished by their eco-friendly attributes including low toxicity, exceptional thermal stability, structurally tunable configurations, and superior charge carrier mobility, have emerged as versatile functional materials in perovskite photovoltaics, particularly for solvent engineering and defect passivation.[11,31,32] Its chemical diversity and tunability make it highly interactive with perovskite materials, laying the foundation for the formation of low-dimensional perovskite.[14] However, the rational design of ionic liquids through optimal cation-anion combinations to synergistically address defect passivation and ion migration suppression remains underexplored.

Herein, we introduced the IL $BPYBF_4$ into the PCBM electron transport layer, where we find that the large cation, BPY^+, interacts with PbI_2 at the interface to form a 1D perovskite structure. This interaction not only effectively passivates the residual PbI_2 defects on the perovskite surface but also establishes a favorable 1D/3D heterojunction that better obstructs ion migration pathways, thereby more effectively mitigating ion migration within the perovskite layer. In comparison to the typical 3D perovskite structure, the 1D/3D mixed dimensional structure exhibits improved stability. Furthermore, BF_4^- forms a chemically resistant anticorrosion layer by coordination with Ag^+, thereby blocking the interaction between Ag^+ and I^- to enhance the corrosion resistance of the Ag electrode and suppressing halogen consumption. Additionally, the introduction of ionic materials optimizes the conductivity of the PCBM layer, thereby improving its electron extraction efficiency. Thanks to these synergistic modification effects, for normal bandgap-based (1.55 eV) PSCs, the IL $BPYBF_4$-modified PSCs achieved a remarkable champion efficiency of 25.28%, significantly outperforming the control group. Furthermore, when stored at 40% relative humidity for 2000 h, the target devices showed excellent stability by retaining 95% of their initial efficiency, while the control devices suffered a substantial efficiency loss, retaining only 62%. Significantly, this passivation strategy demonstrates universal efficacy across wide-bandgap perovskites. Applying the identical strategy to 1.68 and 1.85 eV wide bandgap perovskites elevated the PCE from 21.26% to 22.69% and from 17.19% to 18.60% (with a certified PCE of 17.75%), respectively, providing a robust foundation for enhancing the efficiency of tandem solar cells.

2 | RESULTS AND DISCUSSION

The molecular structure diagram of 1-Butylpyridinium tetrafluoroborate ($BPYBF_4$) is presented in Figure S1, with its corresponding BPY^+ cation electrostatic potential (ESP) mapping depicted in Figure 1A. The pyridinic nitrogen atoms, with their high electronegativity, induce

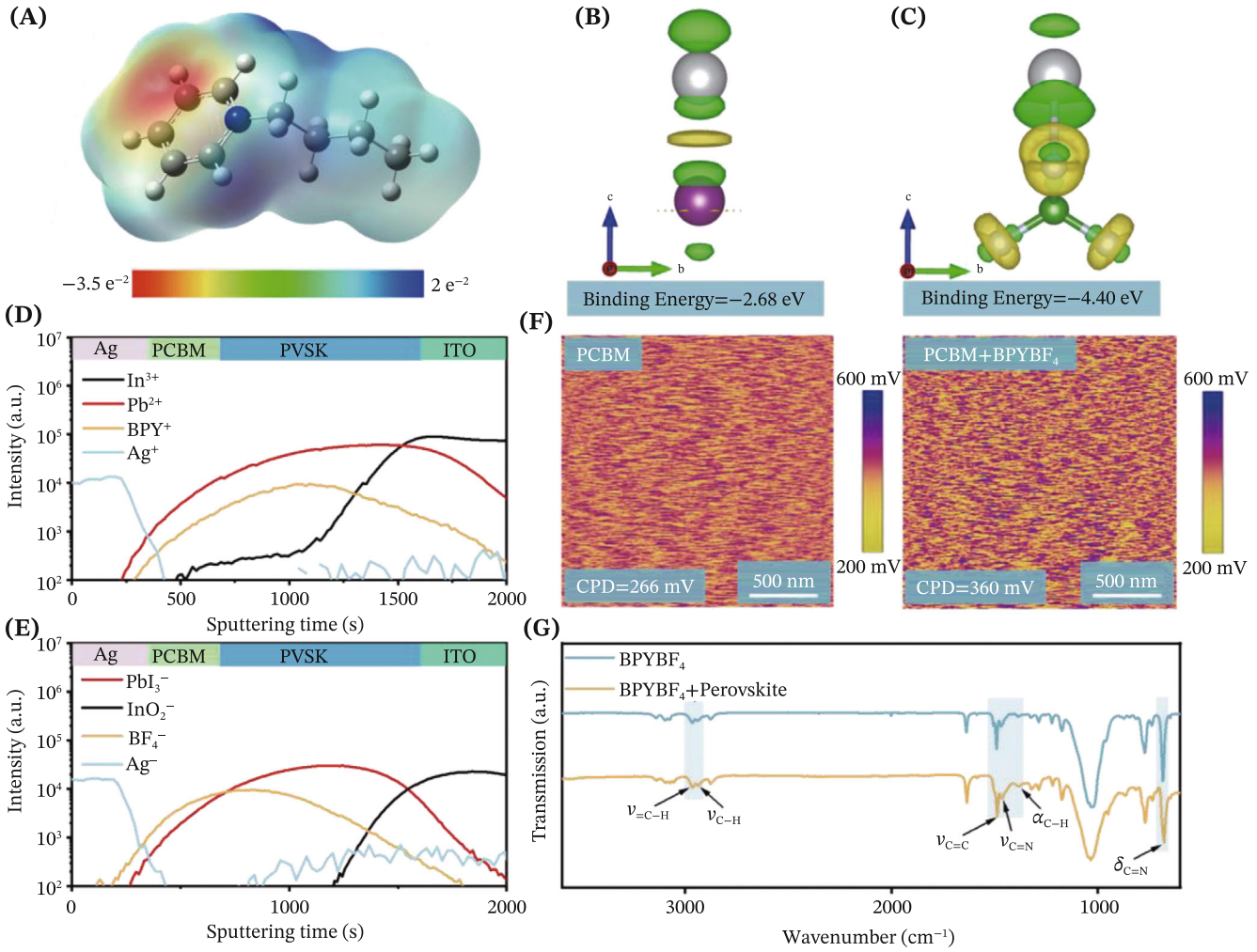

FIGURE 1 (A) Electrostatic potential (ESP) distribution maps of 1-butylpyridine cation. The charge density difference of Ag^+ decorated by (B) I^- and (C) BF_4^- with charge accumulation and depletion represented by green and yellow color. TOF-SIMS depth profile of (D) In^{3+}, Pb^{2+}, BPY^+, Ag^+ and (E) PbI_3^-, InO_2^-, BF_4^-, Ag^- in $BPYBF_4$-treated device (ITO/PVSK/PCBM/Ag). (F) KPFM surface potential images for PCBM with and without $BPYBF_4$ treatment. (G) FTIR spectra of $BPYBF_4$ and $BPYBF_4$ + perovskite.

localized electron density redistribution within the π-conjugated aromatic system, creating electron-rich domains. These nucleophilic regions exhibit strong Lewis base characteristics that effectively passivate undercoordinated Pb^{2+} defects.[33] Concurrently, butyl chains with hydrophobic ability can effectively improve stability.[34] Density functional theory (DFT) calculations were employed to elucidate the inhibitory role of BF_4^- anions in suppressing Ag-I bonding interactions, thereby mitigating halogen depletion. Computational analysis revealed a binding energy of −2.68 eV for the Ag-I complex, whereas the Ag-BF_4^- system exhibited a more thermodynamically favorable binding energy of −4.40 eV. The lower binding energy indicates a stronger affinity between Ag and BF_4^-, effectively inhibiting the chemical interaction between I species and Ag. This suppression of irreversible depletion contributes to improved device efficiency and enhanced long-term operational stability[26] (Figure 1B,C). In addition, the XPS spectra of Ag 3d demonstrates a strong chemical interaction between Ag and $BPYBF_4$, with the Ag $3d_{3/2}$ peak shifting from 374.5 to 374.2 eV, and the Ag $3d_{5/2}$ peak moving from 368.5 to 368.2 eV. This provides compelling evidence for the inhibition of the reaction between metallic Ag and halogens in the perovskite. (Figure S2). Time-of-flight secondary ion mass spectrometry (TOF-SIMS) was conducted to investigate the distribution of IL $BPYBF_4$ in PCBM (Figure 1D,E). The analysis reveals that BPY^+ cations predominantly localize at the perovskite interface through chemical interaction with residual PbI_2, leading to the formation of LD perovskite phase. Meanwhile, BF_4^- anions exhibit a gradient distribution—primarily concentrated at the bottom of PCBM layer for related vacancy passivation, with a small fraction present near

the Ag electrode interface, where they chelate Ag^+ ions. To further verify this hypothesis, we conducted depth-profiling XPS analysis, which conclusively confirmed the spatial distribution mechanism proposed in this study (Figure S3). Additionally, most of the BF_4^- anion distributed at the perovskite surface can effectively occupy iodine vacancies formed during LD perovskite crystallization, owing to their comparable ionic radii.[35] To examine the impact of $BPYBF_4$ on the electrical properties of PCBM films, Kelvin probe force microscopy (KPFM) was performed on both pristine and $BPYBF_4$-treated PCBM films (Figure 1F). The results show that $BPYBF_4$ treatment significantly enhanced the surface potential of the PCBM film from 266 to 360 mV. To assess the conductivity (σ) of the Indium tin oxide (ITO)/PCBM with and without $BPYBF_4$ treatment, a *J–V* test was carried out in the dark (Figure S4). Using the equation: $\sigma = \frac{Jd}{AV}$, where A represents the effective area and d is the thickness of the PCBM layer.[27] The calculated σ values for pristine and $BPYBF_4$-modified PCBM were 3.42×10^{-5} and 8.81×10^{-5} S cm^{-1}, respectively. The enhancement in surface potential and conductivity indicates that the incorporation of $BPYBF_4$ improves electron extraction capability of PCBM while simultaneously mitigating charge carriers accumulation at the interface.[9,29,36] Furthermore, ultraviolet photoelectron spectroscopy (UPS) analysis provides a systematic insight into the $BPYBF_4$-induced energy level realignment (Figure S5). Specifically, the introduction of $BPYBF_4$ drives an upward shift in the conduction band minimum (CBM) of PCBM from −4.37 to −4.19 eV, accompanied by a Fermi level adjustment from −5.08 to −4.98 eV. This favorable energy level alignment effectively optimizes the interfacial CBM offset, thereby facilitating efficient electron extraction while suppressing non-radiative recombination losses. As shown in Figure 1G, Fourier transform infrared spectroscopy (FTIR) measurement was employed to examine the complex interactions between $BPYBF_4$ and the perovskite composites with the corresponding magnified view provided in Figure S6. In the original IL $BPYBF_4$, distinct stretching vibrations (ν) of the ═C—H bond in the pyridine ring are observed at 2966 cm^{-1}, along with the C—H bond in butyl chains at 2939 cm^{-1}. Additionally, C═C and C═N bonds in the pyridine ring, as well as deformation vibration (α) of C—H bonds in the butyl chain, appear at 1490, 1469, and 1386 cm^{-1}, respectively, and the in-plane bending vibration (δ) of C═N in the pyridine ring is observed at 684 cm^{-1}. After introducing perovskite composites, the vibration peaks of $\nu_{=C-H}$, ν_{C-H}, $\nu_{C=C}$, ν_{C-N}, α_{C-H}, and $\delta_{C=N}$ shifted to 2964, 2937, 1487, 1465, 1382, and 688 cm^{-1}, respectively, confirming the interaction between $BPYBF_4$ and the perovskite composites. To further verify the interaction between the ionic liquid and perovskite components, we conducted nuclear magnetic resonance (NMR) measurements. In the ^{1}H NMR spectrum of $BPYBF_4$, the signals between 7 and 10 ppm, attributed to the protons of the aromatic pyridinium ring, exhibited a slight shift upon the addition of perovskite component, indicating a specific interaction between BPY^+ cations and the perovskite species (Figure S7). Additionally, the ^{19}F NMR analysis revealed a pronounced chemical shift in the $BPYBF_4$-perovskite mixture compared to pure $BPYBF_4$ (Figure S8), indicative of F^- coordination to Pb^{2+} centers where BF_4^- partially displaces I^-.[37] To gain a more detailed understanding of this interaction, x-ray photoelectron spectroscopy (XPS) was employed to measure the binding energies of both the control perovskite and the $BPYBF_4$-modified perovskite films (Figure S9). The XPS spectra of C, N, O, Pb and I in the target perovskite films are shown in Figure S10. Upon $BPYBF_4$ modification, both the Pb $4f_{5/2}$ and Pb $4f_{7/2}$ peaks shift to lower binding energies. Specifically, the Pb $4f_{5/2}$ peak moves from 142.9 to 142.8 eV, and the Pb $4f_{7/2}$ peak moves from 138.0 to 137.9 eV. The I 3d characteristic peaks also exhibit a shift: the I $3d_{3/2}$ peak moves from 629.5 to 629.2 eV, and the I $3d_{5/2}$ peak shifts from 618.0 to 617.7 eV, further confirming the strong interaction between $BPYBF_4$ and perovskite composites.

Top-view scanning electron microscopy (SEM) and atomic force microscopy (AFM) were conducted to observe the morphologies of PCBM films with and without $BPYBF_4$ treatment, spin-coated onto perovskite thin films. After introducing $BPYBF_4$, dot-like and rod-like 1D perovskites appeared on the surface of the 3D perovskite (Figure 2A–D). This morphological change is attributed to the strong interaction between $BPYBF_4$ and the residual PbI_2 on the 3D perovskite surface. At a concentration of 2 mg mL^{-1}, larger and more distinct rod-like structures emerged (Figure S11). This evolution in morphology suggests that at lower concentrations, the reaction between the IL and PbI_2 is insufficient, impacting the formation of 1D perovskite.[38] To further confirm these morphological changes, SEM imaging was conducted on perovskite films treated with different concentrations of $BPYBF_4$ (Figure S12). As expected, with lower $BPYBF_4$ concentrations, new dot-like structures appeared on the 3D perovskite surface. Increasing the concentration of $BPYBF_4$ resulted in a greater emergence of rod-like structures, consistent with the earlier observations. To verify that the structures formed at varying IL concentrations are indeed 1D perovskite, x-ray diffraction (XRD) measurements were conducted on PCBM films doped with different concentrations of $BPYBF_4$ (Figure 2E). The films treated with the IL exhibited only new peaks specific to the 1D perovskite, confirming that the observed morphologies at different concentrations correspond to the same

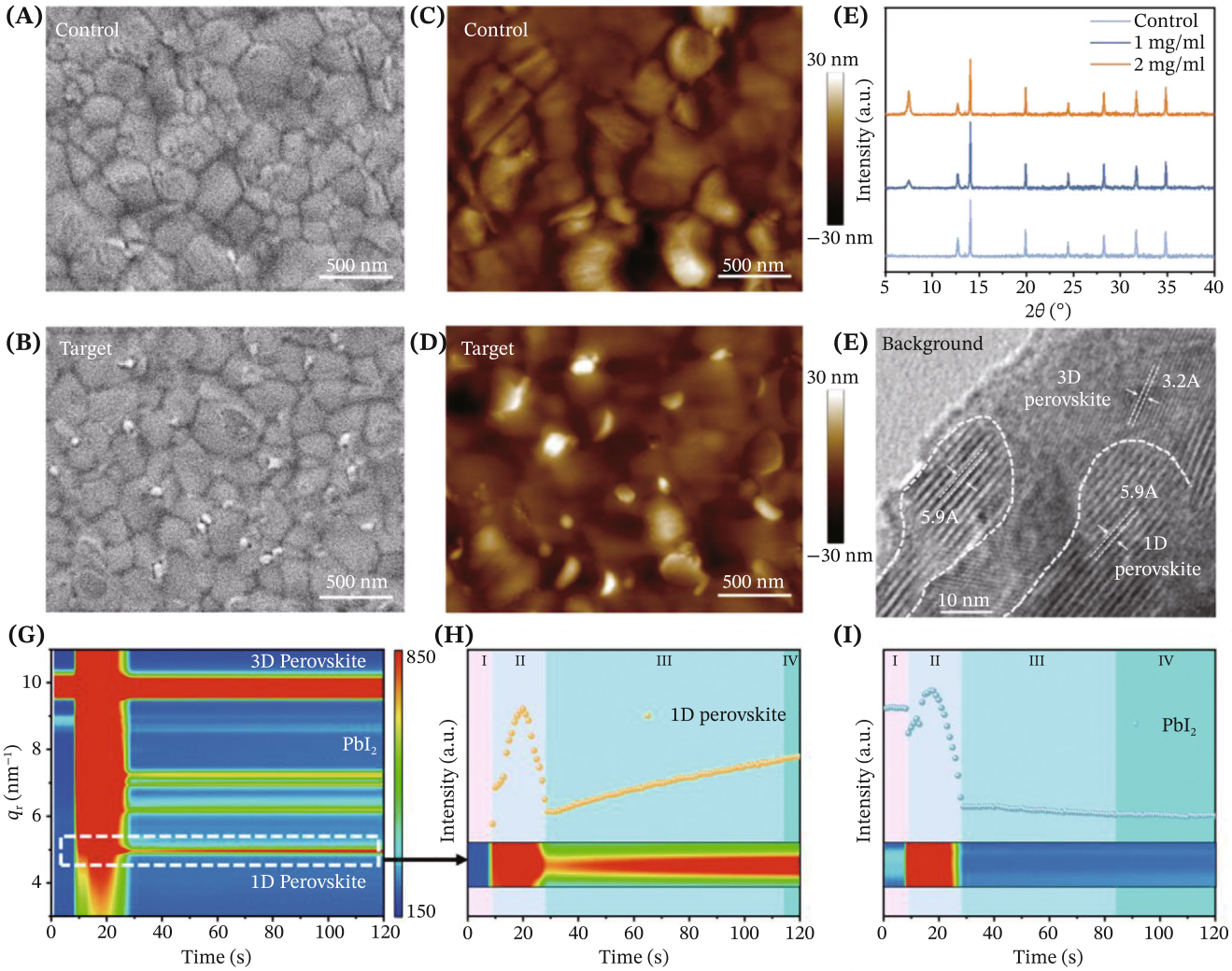

FIGURE 2 (A, B) Top-view SEM images for PVSK/PCBM with and without $BPYBF_4$ treatment. (C, D) AFM topography images for PVSK/PCBM with and without $BPYBF_4$ treatment. (E) XRD patterns for PVSK/PCBM without and with different concentrations of $BPYBF_4$ (1 mg mL^{-1}, 2 mg mL^{-1}) treatment. (F) High-resolution TEM images of 1D/3D hybrid perovskite. (G) Time-resolved GIWAXS spectra. Time evolution of integrated peak intensity of (H) PbI_2 ($q = 9$ nm^{-1}) and (I) 1D perovskite ($q = 5.4$ nm^{-1}) over time.

1D perovskite. Moreover, as the concentration of $BPYBF_4$ increased, the intensity of the 1D perovskite diffraction peaks grew, while the intensity of the PbI_2 diffraction peaks diminished, further indicating the reduction of residual PbI_2 on the film surface due to $BPYBF_4$ treatment. High-resolution transmission electron microscopy (HRTEM) was used to confirm the heterostructure between 1D and 3D perovskite (Figure 2F). The interplanar distance of 3.2 Å corresponds to the 3D perovskite, while the observed interplanar spacing of 5.9 Å in the $BPYBF_4$ region indicates a distinct structural arrangement. Using Bragg's law, $2d\sin\theta = n\lambda$, where d is the interplanar distance, θ is the angle of incidence, n is the order of diffraction (typically 1 in our analyses), and λ is the wavelength of the x-ray (1.54 Å), the interplanar distance was calculated to be 5.9 Å, which aligns with the HRTEM results. To visually track the real-time development of 1D perovskite and the reduction of residual PbI_2, time-resolved grazing-incidence wide-angle x-ray scattering (GIWAXS) experiments were adopted during the thermal annealing process. Figure 2G shows the evolution of the GIWAXS intensity along the q_r direction for the 1D/3D perovskite film over time, capturing the four stages of phase transition including 1D perovskite formation and the disappearance of PbI_2 (Figure 2H,I). In Stage I (0–8 s), the characteristic peaks of 3D perovskite appear at $q = 10$ nm^{-1}, along with a prominent PbI_2 peak at $q = 9$ nm^{-1}, indicating significant residual PbI_2. In Stage II (8–28 s), an increased evaporative signal from the IL solvent is detected, marking the onset of the reaction between the IL and residual PbI_2. During Stage III (28–114 s), the PbI_2 signal levels off while the 1D perovskite

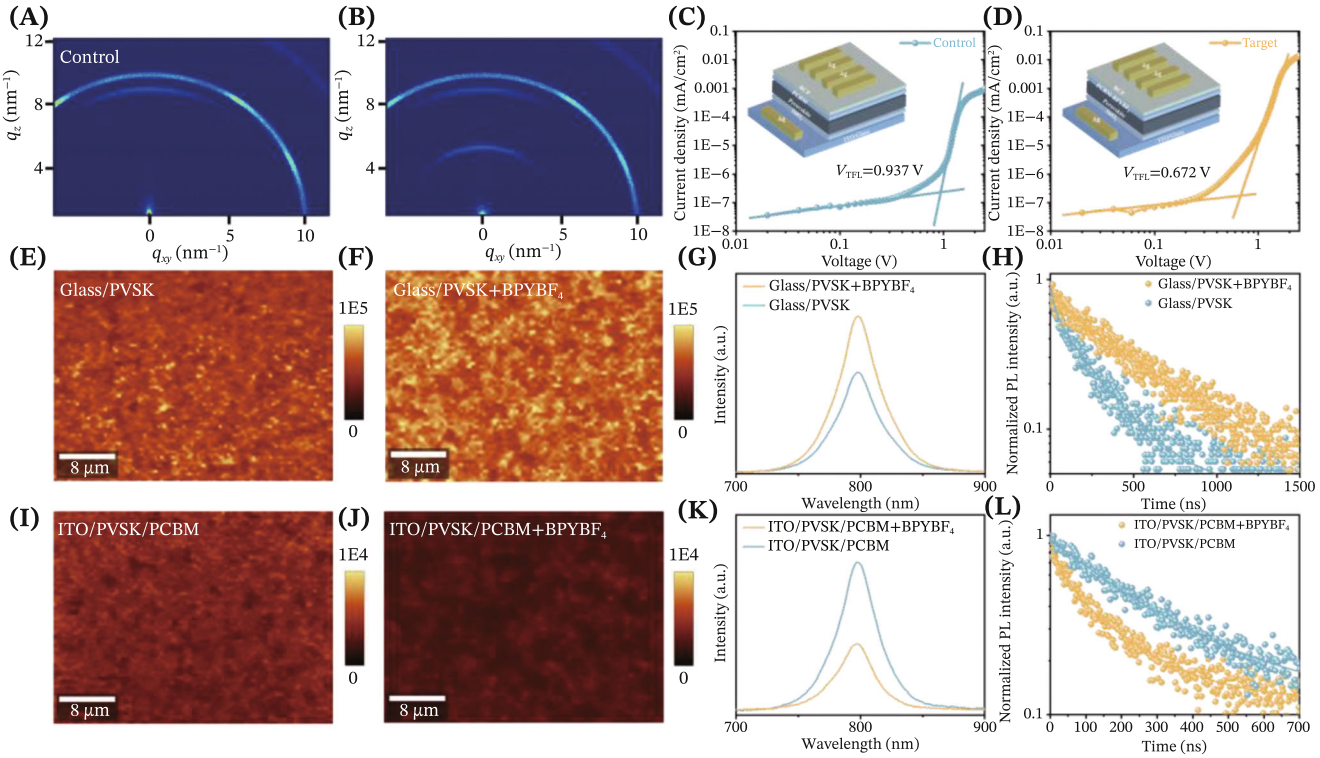

FIGURE 3 The 2D GIWAXS patterns of PVSK/PCBM (A) without and (B) with $BPYBF_4$ treatment. SCLC measurements based on the electron-only device for the (C) control and (D) IL $BPYBF_4$-modified PSCs. PL mapping images of glass/PVSK (E) without and (F) with $BPYBF_4$. (G) PL and (H) TRPL spectra of PVSK films with and without $BPYBF_4$ treatment. PL mapping images of the ITO/PVSK/PCBM (I) without and (J) with $BPYBF_4$. (K) PL and (L) TRPL spectra of PVSK/PCBM with and without $BPYBF_4$ treatment.

signal at $q = 5.4\ \text{nm}^{-1}$ intensifies, indicating the gradual formation of 1D perovskite. In Stage IV (after 114 s), the formation of 1D perovskite reaches completion, with the signals of 3D perovskite, PbI_2, and 1D perovskite stabilizing, confirming the successful transformation.

2D GIWAXS images were obtained to systematically analyze the state of PVSK/PCBM films with and without $BPYBF_4$ treatment. For the control sample, a distinct PbI_2 signal was observed at $q = 9\ \text{nm}^{-1}$ (Figure 3A). However, after the introduction of $BPYBF_4$, a new signal at $q = 5.4\ \text{nm}^{-1}$ emerged, accompanied by a weakening of the PbI_2 signal. This indicates that the residual PbI_2 reacted with $BPYBF_4$, resulting in the formation of 1D perovskite, consistent with the time-resolved GIWAXS results (Figure 3B). The integration of GIWAXS intensities further confirms this trend (Figure S13). To quantify the trap density in both the control and $BPYBF_4$-treated perovskite films, the space-charge-limited current (SCLC) method was employed using a typical electron-only device structure. The trap-filling limit voltage (V_{TFL}) was extracted from the dark-state *I–V* curve of the device (Figure 3C,D), allowing for the calculation of trap densities which can be further calculated by the equation: $N_t = \frac{2\varepsilon_r \varepsilon_0 V_{TFL}}{qL^2}$, where N_t represents the trap density, ε_r represents the relative dielectric constant of the perovskite, ε_0 represents the vacuum dielectric constant, q represents the elementary charge, and L represents the thickness of the perovskite layer. For the $BPYBF_4$-treated perovskite film, the trap density was found to be minimal, as low as $1.09 \times 10^{16}\ \text{cm}^{-3}$, while the control film exhibited a higher trap density of $1.53 \times 10^{16}\ \text{cm}^{-3}$. To systematically benchmark the defect passivation capabilities of $BPYBF_4$, we subsequently selected three representative ionic liquids as PCBM dopants: 1-Methyl-1H-imidazol-3-ium tetrafluoroborate ($MIMBF_4$), N-butylpyridinium hexafluorophosphate ($BPYPF_6$), and N-butyl pyridinium bromide (BPYBr), enabling a controlled investigation through either cationic or anionic substitution. The molecular structures of these ionic liquids are illustrated in Figure S1. The results from SCLC tests show that the N_t values for $MIMBF_4^-$, $BPYBr^-$, and $BPYPF_6^-$ modified films are 1.40×10^{16}, 1.38×10^{16}, and $1.33 \times 10^{16}\ \text{cm}^{-3}$, respectively (Figure S14). These findings provide comprehensive validation for the preeminent surface defect passivation capability of $BPYBF_4$ in perovskite thin films. To explore the impact of $BPYBF_4$-doped PCBM on the properties of perovskite films and charge-carrier transport, confocal photoluminescence (PL) mapping tests were executed to assess the spatial distribution of PL intensity. As shown in Figure 3E–G, the pristine perovskite

exhibited weak PL intensity, whereas the $BPYBF_4$ treated one showed much stronger and more uniform PL signals. This improvement is attributed to the defect passivation of the 3D perovskite by the formed 1D perovskite.[21,39] Notably, when $BPYBF_4$ was employed as the top interface passivation layer for perovskite, it exhibited optimal defect passivation efficacy at a concentration of 1 mg mL^{-1}. In contrast, suboptimal concentrations, whether lower or higher, resulted in diminished effectiveness in suppressing defect-assisted non-radiative recombination (Figure S15). Correspondingly, the $BPYBF_4$-modified perovskite film demonstrated an extended carrier lifetime (Figure 3H and Table S1), indicating a reduction in defects that act as non-radiative recombination centers. Furthermore, for the ITO/perovskite/PCBM devices with and without $BPYBF_4$ treatment, electron quenching in the pristine sample exhibited severe hysteresis, which can be attributed to the limited ability of the control PCBM to extract electrons. In contrast, the $BPYBF_4$-treated sample displayed more rapid electron quenching and improved uniformity, signifying a significant enhancement in electron extraction efficiency (Figure 3I–K).[29,40] Consistently, the incorporation of $BPYBF_4$ at a concentration of 1 mg mL^{-1} exhibits the most favorable electron extraction efficiency (Figure S16). The decrease in carrier lifetime further corroborates the optimization of charge extraction from PCBM by $BPYBF_4$ (Figure 3L and Table S2). PL characterization reveals that $BPYBF_4$-incorporated devices exhibit the lowest PL intensity among all samples, confirming its superior efficacy in perovskite surface defect passivating and charge transport enhancement (Figure S17).

To evaluate the photovoltaic performance, inverted perovskite solar cells with a p-i-n architecture were fabricated (Figure S18) and the cross-section SEM was shown in Figure S19, where the PCBM electron-transport layer was strategically functionalized with $BPYBF_4$ to enhance interfacial passivation. Notably, a systematic approach was implemented to validate the universality of our optimization strategy. Perovskite absorbers with engineered bandgaps were employed as photoactive layers, including: (i) normal-bandgap (NBG) (1.55 eV), (ii) wide-bandgap (WBG) (1.67 eV), and (iii) WBG (1.85 eV) compositions, spanning the spectral range of photovoltaic relevance. To optimize the device performance of 1.55 eV PSCs, we investigated the impact of $BPYBF_4$ concentration with the corresponding photovoltaic parameters presented in Figure S20. The NBG 1.55 eV PSCs device treated with the optimal concentration of $BPYBF_4$ exhibited significant improvements in photovoltaic performance, achieving a champion PCE of 25.28%, with an open-circuit voltage (V_{OC}) of 1.151 V, a short-circuit current (J_{SC}) of 25.58 mA cm^{-2}, and a fill factor (FF) of 85.87%. In comparison, the control device reached a champion PCE of only 23.26% (Figure 4A). *J–V* curves of PSCs modified with other ILs-modified are presented in Figure S21. Devices incorporating $MIMBF_4$, BPYBr and $BPYPF_6$ achieved champion PCEs of 23.90%, 24.60%, and 24.76%, respectively, with detailed photovoltaic parameters summarized in Table S3. Notably, $BPYBF_4$ delivers the highest performance enhancement, further confirming its superior interfacial modification capability as elucidated in the preceding discussion. The universal efficacy of our optimization strategy has been systematically validated across PSCs employing wide-bandgap absorbers, particularly demonstrating remarkable effectiveness in devices with 1.67 and 1.85 eV perovskite compositions. SEM imaging reveals ubiquitous rod-like 1D phases on both 1.67 and 1.85 eV perovskite surfaces, as structurally corroborated by XRD and GIWAXS (Figure S22–S24). As demonstrated in Figure 4B and Table S4, $BPYBF_4$ functionalization enables a significant enhancement in PCE from 21.26% to 22.69% for WBG 1.67 eV PSCs, accompanied by concomitant improvements in all photovoltaic parameters. Furthermore, the $BPYBF_4$ modification strategy demonstrates pronounced optimization effects in WBG 1.85 eV PSCs, elevating the PCE from 17.19% to 18.60%. This enhancement is accompanied by a substantial increase in V_{OC} and FF, alongside a marginal improvement in J_{SC} (Figure 4C and Table S5). Under *J–V* measurement, the certified PCE of the target WBG 1.85 eV PSCs was confirmed as 17.75% (Figure S25). A summary of the certified PCE values for single-junction WBG PSCs (above 1.6 eV) reported in the literature is shown in Figure 4D and Table S6. Notably, this marks the first certification of WBG PSCs above 1.8 eV. These results indicated that our strategy suits both NBG (1.55 eV) and WBG (1.67 and 1.85 eV)-PSCs. External quantum efficiency (EQE) test was conducted to evaluate the current matching mechanism (Figure S26). Specifically, the integrated J_{sc} values of the champion PSCs with different bandgaps perovskite materials of 1.55, 1.67, and 1.85 eV are 24.51, 20.30, and 16.96 mA cm^{-2}, respectively. Statistical analysis of photovoltaic parameters across compositionally diverse devices, as systematically compiled in Figure 4E, demonstrates unambiguously that $BPYBF_4$ modification universally enhances all performance parameters of PSCs. This comprehensive dataset validates the generalizability and broad applicability of the $BPYBF_4$ optimization strategy for different bandgaps-based PSCs. Additionally, conventional Mott–Schottky measurements were conducted to investigate the specific factors contributing to the performance enhancement (Figure 4F). These measurements revealed that after the introduction of $BPYBF_4$, the built-in potential (V_{bi}) was significantly elevated, suggesting

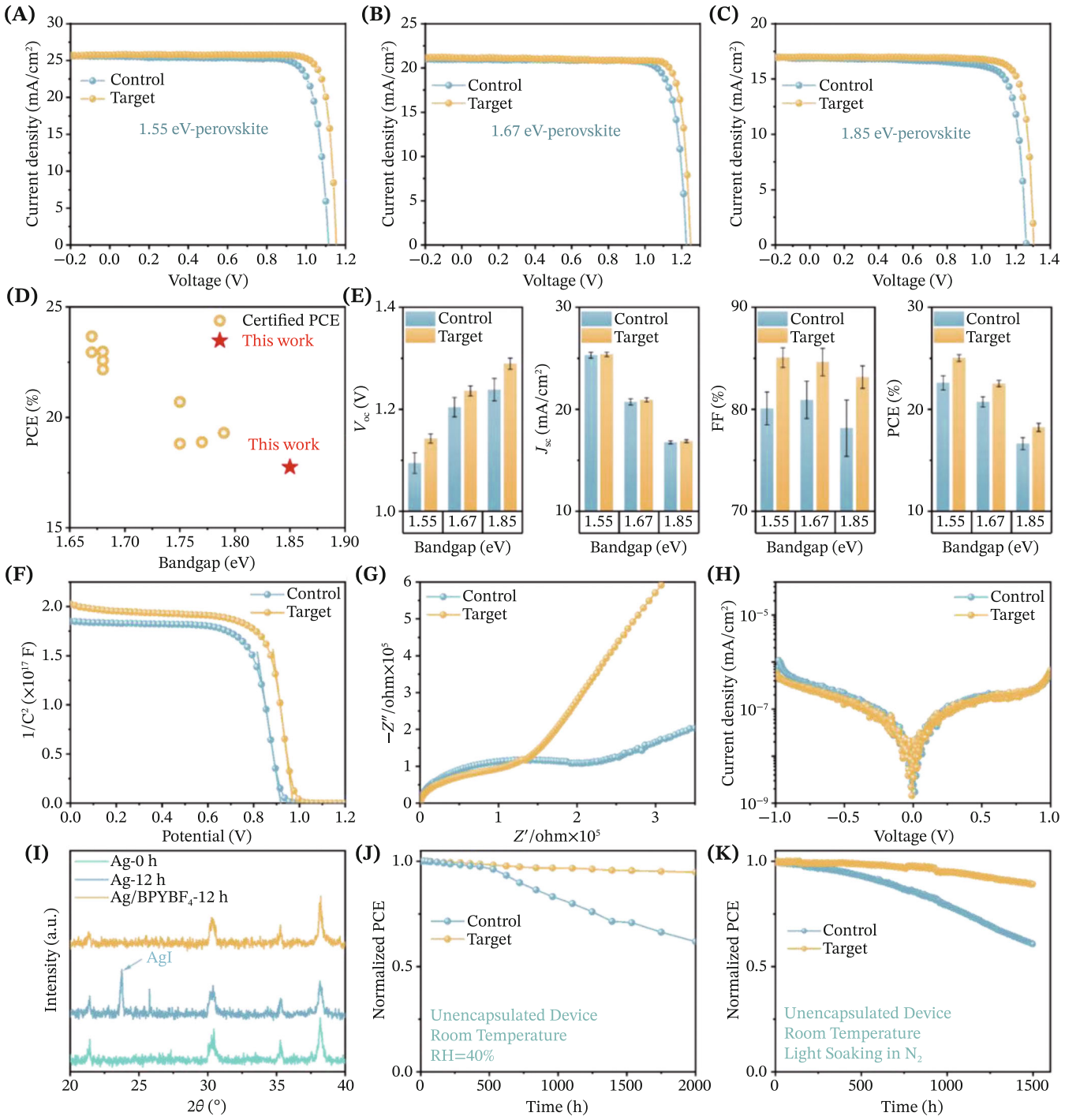

FIGURE 4 Champion *J–V* curves of control and target (A) 1.55 eV, (B) 1.67 eV, and (C) 1.85 eV PSCs devices. (D) Summary of certified PCE value of wide bandgap PSCs reported in the literature (above 1.6 eV). (E) The column-shaped statistical chart of V_{oc}, J_{sc}, FF, and PCE parameters for control and target devices based on 1.55 eV, 1.67 eV, and 1.85 eV perovskite as photoactive layer. (F) Mott–Schottky pattern, (G) Nyquist plots, and (H) Dark *J–V* curves of control and target PSCs. (I) XRD patterns for Ag film following varying periods of immersion in $FAPbI_3$ dispersion. (J) Normalized PCE of unencapsulated 1.55 eV PSCs exposure at 25°C under 40% RH condition over 2000 h. (K) Normalized PCE of unencapsulated 1.55 eV PSCs under continuous illumination at N_2 atmosphere over 1500 h.

improved charge transport characteristics and charge-carrier extraction capacity, leading to higher values of V_{oc} and FF.[41] Electrochemical impedance spectroscopy (EIS) measurements were then carried out under a 0 V bias condition (Figure 4G). In the EIS curves, the arcs observed in the high-frequency and low-frequency regions correspond to the charge transfer resistance and the charge recombination resistance, respectively.

Compared to the control devices, the $BPYBF_4$-modified devices showed reduced charge transfer resistance and increased charge recombination resistance, indicating enhanced charge transfer performance and reduced non-radiative recombination. Moreover, the device modified with $BPYBF_4$ exhibited a lower dark current density, further signifying improved charge transport performance benefited by the regulation of energy levels and reduced leakage current, which is intrinsically linked to the effective modification of PCBM (Figure 4H). The 1D/3D heterojunction structure not only contributed to the improvement of the PCE of PSCs but also enhanced their stability. De-ionized water contact angle tests were applied to investigate the impact of 1D perovskite on the hydrophobicity of 3D perovskite thin films (Figure S27). The results revealed that the contact angle increased from 62° for the pristine film to 77° for the 1D/3D films. A larger contact angle provides compelling evidence of increased hydrophobicity, which in turn suggests a significant enhancement in the water-resistance ability and humidity stability of 3D perovskite thin films. This improvement is primarily attributed to the stable structural characteristics of 1D perovskite, which forms a more robust water-resistant barrier for the 3D perovskite films. To mechanistically unravel the enhanced stability of 1D/3D perovskite heterostructures, we performed in-situ PL measurements under controlled conditions (25°C, 40% RH) (Figure S28). Quantitative analysis reveals the 3D perovskite experiences rapid defect generation, as indicated by a PL intensity decline to approximately 49% of its initial value. In contrast, the 1D/3D perovskite films demonstrate markedly improved stability, retaining nearly 95% of their initial PL intensity after 1000 s, confirming the effective suppression of ion migration.[42] Inductively coupled plasma mass spectrometry (ICP-MS) tests were conducted to further illustrate the enhancement of water resistance in 3D perovskite thin films upon incorporation of 1D perovskite. Both 3D and 1D/3D perovskite films were immersed in DI water for various duration (30, 60, 180, and 300 s) (Figure S29). The ICP-MS results showed a notable reduction in lead leakage from 1D/3D perovskite films compared to 3D perovskite films. As the immersion time increased, the improvement in water-resistance became increasingly evident, reflected in the growing difference in Pb^{2+} concentration in the solution. This enhanced humidity resistance ability is attributed to the passivation of surface defects and the suppression of ion migration by 1D perovskite. In-situ UV–vis absorption measurements were conducted to assess the thermal stability of perovskite films with and without $BPYBF_4$ treatment over time. As seen in Figure S30, the 3D perovskite exhibited poor stability, with a gradual reduction in UV–vis absorption after exposure to 200°C and 60% RH. In the 600 nm wavelength region, the UV–vis absorption intensity significantly decreased after 600 s of heating. In contrast, the UV–vis absorption intensity of the 1D/3D sample displayed remarkable stability, suggesting outstanding light absorption stability. These results underscore the critical role of IL doping in PCBM, which facilitates the formation of 1D perovskite and significantly enhances the stability of the perovskite layer. To highlight the protective role of BF_4^- in preventing the formation of AgI, which can be detrimental, we designed an immersion experiment simulating the interaction between Ag and I in a realistic environment using components from the perovskite ternary system: FA^+ ($CH(NH_2)_2^+$), I^-, and Pb^{2+} (lead ion). As depicted in Figure S31, we immersed the ITO/Ag in a $FAPbI_3$ dispersion prepared by dissolving PbI_2 and FAI in isopropyl alcohol to produce a concentrated $FAPbI_3$ dispersion (50 mg mL^{-1}). After soaking for 12 h in pure perovskite dispersion, the Ag film became rough and lost its metallic luster, indicating corrosion due to the I-rich environment. In contrast, when the Ag film was immersed in the perovskite dispersion solution containing $BPYBF_4$ (1 mg mL^{-1}), only slight changes in color were observed even after 12 h. XRD analysis of fresh and degraded Ag films (with and without $BPYBF_4$) revealed that immersion in the perovskite dispersion led to the appearance of an AgI peak in the XRD pattern, indicating chemical corrosion of Ag (Figure 4I). However, when Ag was immersed in the perovskite solution containing $BPYBF_4$, no AgI diffraction peak was detected, demonstrating that $BPYBF_4$ effectively prevents the formation of AgI. To conclusively validate our findings, post-immersion Ag samples were rinsed with IPA and analyzed by energy dispersive spectrometer (EDS) elemental mapping. The control samples exhibited significant Ag depletion accompanied by substantial iodine infiltration, indicative of severe AgI corrosion. In sharp contrast, $BPYBF_4$-modified samples retained surface Ag with minimal iodine presence, clearly demonstrating the suppression of halide-induced metal degradation (Figure S32). These observations are consistent with our DFT calculations, further confirming that BF_4^- preferentially coordinates with Ag^+, effectively mitigating the corrosive effect of I^- on the Ag electrode. This protective effect is crucial for maintaining the stability of the metal electrode in the device and suppressing halogen consumption in the perovskite. Moreover, we assessed the long-term stability of the devices by tracking the attenuation of device efficiency for 2000 h at room temperature and 40% RH (Figure 4J). Remarkably, the $BPYBF_4$-modified devices retained 95% of their initial PCE after 2000 h, whereas the control devices experienced significant efficiency losses, maintaining only 62%

of their initial value. Additionally, we evaluated the photo-stability of the devices under continuous illumination in a N_2 atmosphere (Figure 4K). The $BPYBF_4$-modified devices demonstrated excellent light degradation resistance, maintaining 89% of their initial PCE after 1500 h, while the control devices exhibited faster degradation, retaining only 61% of their original PCE, further highlighting the effectiveness of the modification. Concurrently, we performed stability tests on both unencapsulated 1.67 and 1.85 eV PSCs under ambient conditions (25°C, 40% RH) to evaluate the general application of the stability enhancement conferred by $BPYBF_4$ modification (Figure S33). After 600 h of aging, the $BPYBF_4$-modified 1.67 eV device retained approximately 96% of its initial PCE, significantly outperforming the control device, which exhibited 88% retention. Similarly, the $BPYBF_4$-modified 1.85 eV device maintained 96% of its original efficiency after the same duration, while the control counterpart retained only 86%.

3 | CONCLUSION

In summary, we introduced the IL $BPYBF_4$ into the PCBM layer, where the BPY^+ cations engage in strong chemical interactions with perovskite components to spontaneously form 1D/3D mixed-dimensional perovskite films, while the BF_4^- anions coordinate with Ag^+ to effectively stabilize halides in the perovskite lattice. We employed time-resolved GIWAXS to elucidate the dynamic formation mechanism of one-dimensional perovskite and the in-situ formation of 1D perovskites significantly optimizes the 3D perovskite film quality, as evidenced by reduced trap-state density and homogenized PL intensity. Crucially, DFT calculations reveal a stronger binding affinity between BF_4^- and Ag^+ compared to I^-, which is pivotal in retarding perovskite degradation pathways. Furthermore, the IL incorporation elevates the PCBM surface potential and enhances its electrical conductivity, synergistically promoting electron extraction efficiency and suppressing carrier non-radiative recombination. This dual-functional doping strategy achieves a champion PCE of 25.28% for 1.55 eV bandgap PSCs with exceptional stability, while simultaneously boosting the efficiencies of 1.68 and 1.85 eV wide-bandgap counterparts to 22.69% and 18.60% (certified as 17.75%), respectively.

ACKNOWLEDGMENTS

This work is funded by Nazarbayev University under Collaborative Research Program (Grant No. 211123CRP1613, A. N.); Faculty Development Competitive Research Grants Program for 2024–2026 (Grant No. 201223FD8801, A. N.). This work is supported by Scientific Research Startup Fund for Spray-on Perovskite Photovoltaics R&D Center (No. 602331011PQ) and Research Projects of Department of Education of Guangdong Province (2024ZDZX3079). The financial support from Guangdong Basic and Applied Basic Research Foundation (No. 2023A1515011677), the Scientific and Technical Innovation Council of Shenzhen (20220812165832002), Research Projects of Department of Education of Guangdong Province (2023GCZX015), and the Innovation Team Project of Guangdong (2022KCXTD055) is gratefully acknowledged. Chunming Yang thanks the National Key R&D Program of China (2021YFA1601000), the Shanghai Municipal Science and Technology Major Project, and the National Natural Science Foundation of China (Grant Nos. 12175295 and U1932118) for support.

CONFLICT OF INTEREST STATEMENT

The authors declare no conflict of interest.

ORCID

Hanlin Hu https://orcid.org/0000-0001-5617-0998

REFERENCES

1. Zhang M, Lan S, Yang BB, et al. Ultrahigh energy storage in high-entropy ceramic capacitors with polymorphic relaxor phase. *Science*. 2024;384(6692):185.
2. Yang Y, Chen H, Liu C, et al. Amidination of ligands for chemical and field-effect passivation stabilizes perovskite solar cells. *Science*. 2024;386(6724):898.
3. Zhang Z, Chen W, Jiang X, et al. Suppression of phase segregation in wide-bandgap perovskites with thiocyanate ions for perovskite/organic tandems with 25.06% efficiency. *Nat Energy*. 2024;9(5):592-601.
4. Liu Z, Xiong Z, Yang S, et al. Strained heterojunction enables high-performance, fully textured perovskite/silicon tandem solar cells. *Joule*. 2024;8(10):1.
5. Zhou J, Fu S, Zhou S, et al. Mixed tin-lead perovskites with balanced crystallization and oxidation barrier for all-perovskite tandem solar cells. *Nat Commun*. 2024;15(1):2324.
6. Ye S, Rao H, Feng M, et al. Expanding the low-dimensional interface engineering toolbox for efficient perovskite solar cells. *Nat Energy*. 2023;8(3):284-293.
7. Azmi R, Ugur E, Seitkhan A, et al. Damp heat–stable perovskite solar cells with tailored-dimensionality 2D/3D heterojunctions. *Science*. 2022;376(6588):73.
8. Yoo JJ, Seo G, Chua MR, et al. Efficient perovskite solar cells via improved carrier management. *Nature*. 2021;590(7847):587-593.
9. Sun X, Li Y, Liu D, et al. VOC of inverted perovskite solar cells based on N-doped PCBM exceeds 1.2 V: Interface energy alignment and synergistic passivation. *Adv Energy Mater*. 2023;13(41):2302191.
10. Yang D, Zhang X, Wang K, et al. Stable efficiency exceeding 20.6% for inverted perovskite solar cells through polymer-optimized PCBM electron-transport layers. *Nano Lett*. 2019;19(5):3313-3320.

11. Wang F, Wang T, Sun Y, et al. Two-step perovskite solar cells with > 25% efficiency: Unveiling the hidden bottom surface of perovskite layer. *Adv Mater*. 2024;36:2401476.
12. Jiang Q, Zhao Y, Zhang X, et al. Surface passivation of perovskite film for efficient solar cells. *Nat Photonics*. 2019;13(7):460-466.
13. Du Y, Tian Q, Wang S, et al. Crystallization control based on the regulation of solvent–perovskite coordination for high-performance ambient printable $FAPbI_3$ perovskite solar cells. *Adv Mater*. 2024;36:2307583.
14. Wang F, Zhou K, Zhou C, et al. Ionic liquid-induced 1D perovskite: exploring 1D perovskite structure to 1D/3D heterojunction-based photovoltaics. *Adv Energy Mater*. 2024;14(23):2400021.
15. Kong T, Xie H, Zhang Y, et al. Perovskitoid-Templated formation of a 1D@3D perovskite structure toward highly efficient and stable perovskite solar cells. *Adv Energy Mater*. 2021;11(34):2101018.
16. Li B, Liu Q, Gong J, et al. Harnessing strong aromatic conjugation in low-dimensional perovskite heterojunctions for high-performance photovoltaic devices. *Nat Commun*. 2024;15(1):5879.
17. Li DB, Yao C, Vijayaraghavan SN, et al. Low-temperature and effective ex situ group V doping for efficient polycrystalline CdSeTe solar cells. *Nat Energy*. 2021;6(7):715-722.
18. Liu H, Zhang Z, Fang J, et al. Eliminating over-oxidation of ruthenium oxides by niobium for highly stable electrocatalytic oxygen evolution in acidic media. *Joule*. 2023;7(3):558-573.
19. Liu C, Yang Y, Chen H, et al. Two-dimensional perovskitoids enhance stability in perovskite solar cells. *Nature*. 2024;633(8029):359-364.
20. Ye F, Tian T, Su J, et al. Tailoring low-dimensional perovskites passivation for efficient two-step-processed $FAPbI_3$ solar cells and modules. *Adv Energy Mater*. 2024;14(4):2302775.
21. Ji R, Zhang Z, Deconinck M, et al. Spontaneous formation of 1D/3D perovskite heterojunctions for efficient inverted perovskite solar cells. *Adv Energy Mater*. 2024;14(20):2304126.
22. Chen Q, Deng K, Shen Y, Li L. Stable one dimensional (1D)/three dimensional (3D) perovskite solar cell with an efficiency exceeding 23%. *InfoMat*. 2022;4(5):e12303.
23. Yang WS, Noh JH, Jeon NJ, et al. High-performance photovoltaic perovskite layers fabricated through intramolecular exchange. *Science*. 2015;348(6240):1234.
24. Gong C, Li H, Wang H, et al. Silver coordination-induced n-doping of PCBM for stable and efficient inverted perovskite solar cells. *Nat Commun*. 2024;15(1):4922.
25. Zhao Y, Yavuz I, Wang M, et al. Suppressing ion migration in metal halide perovskite via interstitial doping with a trace amount of multivalent cations. *Nat Mater*. 2022;21(12):1396-1402.
26. Li X, Fu S, Zhang W, Ke S, Song W, Fang J. Chemical anti-corrosion strategy for stable inverted perovskite solar cells. *Sci Adv*. 2020;6(51):eabd1580.
27. Li Y, He X, Zhu R, et al. Enhanced corrosion resistance of Ag electrode through ionized 2-Mercaptobenzothiazole in inverted perovskite solar cells. *Adv Funct Mater*. 2024;35(3);2413245.
28. Ning J, Zhu Y, Hu Z, et al. Gaining insight into the effect of organic Interface layer on suppressing ion migration induced interfacial degradation in perovskite solar cells. *Adv Funct Mater*. 2020;30(35):2000837.
29. Gong C, Li H, Xu Z, et al. Efficient and stable inverted perovskite solar cells enabled by homogenized PCBM with enhanced electron transport. *Nat Commun*. 2024;15(1):9154.
30. Li H, Xie G, Fang J, et al. Holistic dielectric and buffer interfacial layers enable high-efficiency perovskite solar cells and modules. *Nano Energy*. 2024;124:109507.
31. Li M, Zhao C, Wang ZK, et al. Interface modification by ionic liquid: a promising candidate for indoor light harvesting and stability improvement of planar perovskite solar cells. *Adv Energy Mater*. 2018;8(24):1801509.
32. Niu T, Chao L, Gao W, et al. Ionic liquids-enabled efficient and stable perovskite photovoltaics: Progress and challenges. *ACS Energy Lett*. 2021;6(4):1453-1479.
33. Yin L, Huang W, Fang J, et al. Crystallization control for ambient printed FA-based lead triiodide perovskite solar cells. *Adv Mater*. 2023;35:2303384.
34. Sun Y, Wang F, Lu L, et al. Enhancing the humidity resistance of perovskite photovoltaics: comprehensive PbI_2 management utilizing long-chain ionic liquid. *Nano Energy*. 2025;136:110716.
35. Bai S, Da P, Li C, et al. Planar perovskite solar cells with long-term stability using ionic liquid additives. *Nature*. 2019;571(7764):245-250.
36. Kayesh ME, Karim MA, He Y, Shirai Y, Yanagida M, Islam A. Minimization of energy level mismatch of PCBM and surface passivation for highly stable Sn-based perovskite solar cells by doping n-type polymer. *Small*. 2024;20(43):2402896.
37. Nagane S, Macpherson S, Hope MA, et al. Tetrafluoroborate-Induced reduction in defect density in hybrid perovskites through halide management. *Adv Mater*. 2021;33:2102462.
38. Wang T, Wang F, Sun Y, et al. Ionic liquid top surface engineering: In situ GIWAXS insights into 1D/3D heterojunction perovskite formation. *Small Methods*. 2024;2401852.
39. Lin J, Huang R, Peng X, et al. Eliminating hole extraction barrier in 1D/3D perovskite heterojunction for efficient and stable carbon-based $CsPbI_3$ solar cells with a record efficiency. *Adv Mater*. 2024;36:2404561.
40. Wang Y, Lin R, Liu C, et al. Homogenized contact in all-perovskite tandems using tailored 2D perovskite. *Nature*. 2024;635(8040):867-873.
41. Qiu J, Mei X, Zhang M, et al. Dipolar chemical bridge induced $CsPbI_3$ perovskite solar cells with 21.86 % efficiency. *Angew Chem Int Ed Engl*. 2024;63(18):e202401751.
42. Zhao Y, Xiang H, Ran R, Zhou W, Wang W, Shao Z. Beyond two-dimension: one- and zero-dimensional halide perovskites as new-generation passivators for high-performance perovskite solar cells. *J Energy Chem*. 2023;83:189-208.

SUPPORTING INFORMATION

Additional supporting information can be found online in the Supporting Information section at the end of this article.

How to cite this article: Sun Y, Ma Q, Wang F, et al. Bidirectional functionality of a modified PCBM layer: Enhancing perovskite photovoltaics beyond single-bandgap devices. *InfoMat*. 2025;7(10):e70043. doi:10.1002/inf2.70043